Electron Beam Lithography for contacting single nanowires on non-flat suspended substrates

Jordi Samà[a,b], Guillem Domènech-Gil[a,b], Isabel Gràcia[c], Xavier Borrisé[c], Carles Cané [c], Sven Barth[d], Frederik Steib[e], Andreas Waag[e], Joan-Daniel Prades[a,b], Albert Romano-Rodríguez[a,b,*]

[a]*Institute of Nanoscience and Nanotechnology (IN²UB), Universitat de Barcelona (UB), c/Martí i Franquès 1, 08028 Barcelona, Spain.*
[b]*MIND-Department of Electronic and Biomedical Engineering, Universitat de Barcelona (UB), c/Martí i Franquès 1, 08028 Barcelona, Spain.*
[c]*Institut de Microelectrònica de Barcelona, Centre Nacional de Microelectrònica, Consejo Superior de Investigaciones Científicas, (IMB-CNM-CSIC), Campus UAB, 08193 Bellaterra, Spain.*
[d]*Institute of Materials Chemistry, TU Wien, Getreidemarkt 9, 1060 Vienna, Austria.*
[e]*Institut für Halbleitertechnik and Laboratory for Emerging Nanometrology, Technische Universität Braunschweig, 38092 Braunschweig, Germany.*

* Corresponding author.
E-mail address: aromano@el.ub.edu
Tel.: +34-934039156.

Abstract

A methodology based on the use of Electron Beam Lithography for contacting individual nanowires on top of non-flat micromembranes and microhotplates has been implemented, and the practical details have been exhaustively described. The different fabrication steps have been adapted to the substrate's topology, requiring specific holders and conditions. The methodology is demonstrated on individual SnO_2 nanowires, which, after fabrication, have been characterized as functional resistive gas nanosensors towards NH_3 and benchmarked against similar devices fabricated using more conventional Dual Beam Focused Ion Beam techniques, demonstrating the superior properties of the here presented methodology, which can be further extended to other non-conventional suspended substrates and nanomaterials.

1. Introduction

Engineered nanomaterials, like nanotubes, nanowires, nanorods, etc. can be tailored to meet the needs of many applications in chemistry, physics, biology, and electronics [1–3]. As a result, they are nowadays becoming key elements in the design and production of advanced microsystems and devices [4]. In electronic engineering, these nanomaterials are being integrated using existing microfabrication technologies to develop the prototypes of tomorrow's electronic devices. The development of such prototypes is still an open challenge with a number of unsolved fabrication issues [5,6].

Among them, and specifically when dealing with individual nanostructures, the fabrication of electrical contacts are widely performed by the most advanced direct writing nanofabrication techniques to provide high spatial resolution and flexibility to operate on a wide range of device layouts, nanomaterial shapes and sizes, and substrate properties, in order to ensure the electrical conduction through a reliable contact [7].

Concerning the use of individual nanostructures, and specifically nanowires, one of the most deeply explored application is sensing, and among these, resistive nanowire-based gas sensors are of significant interest due to their high surface-to-volume ratio, which enhances the interaction between the nanostructure and the surrounding gas atmosphere, but also due to their relatively simple measurement and operation mechanisms [8].

The construction of such gas sensing devices starts with the transfer of the nanowires from the initial growth substrate to a microelectronic platform, containing electrodes and signal

conditioning elements, like heaters, temperature sensors, etc. To date, this removal and transfer is mostly performed manually. There have been reported successful attempts to grow directly the nanowires on top of the sensing platforms [9,10], but it has only be possible to grow bundles and not individual nanowires; although, there are also initiatives in this direction [11].

Once the nanowires lay on the final substrate, they need to be accessed electrically. This issue has been mostly addressed for flat substrates. In the most advanced devices, however, the substrates consist of complex suspended microstructures designed to optimize other operation properties, like the power needed to reach the optimum working temperature. These patterned substrates present a non-negligible surface roughness and can be strongly bent. In these conditions, electrode fabrication was only possible to date with dual-beam focused ion beam systems, employing the electron- and/or ion-sources to decompose a metal-organic gas precursors, like PtC_9H_{16}, to locally deposit a metal-like platinum/carbon composite, with high spatial resolution [12,13]. This process allowed for the fabrication of nano-contacts to the individual nanowires through a direct and mask-less process [14], and could cope with the surface variations of rough, non-flat substrates, like the aforementioned microhotplates or micromembranes, with an embedded heater [15].

However, the technique is time consuming, requiring few hours to fabricate the contacts to one single nanowire, and most of the metalorganic precursors employed for this purpose gave rise to important amounts of carbon in the deposit, which were responsible for high resistance and limited thermal stability, as the deposited contact material started to evaporate and degrade at about 400 °C [16].

As an alternative, electron beam lithography (EBL) is a resist patterning technique which can achieve very high resolution (down to few nanometres) and which can be used on large area substrates (up to 8" wafers). Its combination with thermal evaporation or magnetron sputtering of metals, followed by a lift-off process, also allows for the fabrication of nano-contacts. In this way, individual nanowires were successfully contacted [17–19], resulting e.g. in field effect transistors that use the nanowires as the channel [20]. Few works are found, however, reporting resistive gas sensors based on individual nanowires fabricated with EBL. Instead, nano-trenches defined by EBL were etched on previously deposited films of TiO_2 [21] or SnO_2 [22] to fabricate nanostrip-like metal oxide gas sensors. These strips are, in contrast to the desired bottom-up synthesized nanowires, polycrystalline and their width is usually much larger, giving rise to a smaller effective surface-to-volume ratio. However, all these works were carried out on flat substrates that contained no efficient means to heat up the sensor material [23–26]. If rough, bent, and non-flat substrates come into play, standard EBL processing fails to provide the required fabrication capabilities. In this context, a thorough study, analysing how the EBL process can be adapted and optimized to operate well on non-flat substrates, is much sought after.

On the other hand, some papers can be found in literature in which the authors report that contacts for the individual nanowires are fabricated without a direct writing method on top of the nanostructure. The techniques are based, among others, on locating the nanowires on pre-patterned electrodes, applying an external electric field using dieletrophoretic alignment [27], using lithographically patterned nanowire electrodeposition [28] or laser ablation combined with photolithography [29].

In this work, we present a methodology to fabricate electrical contacts on individual nanowires laying on top of strongly bent and rough microhotplates and micromembranes by means of EBL. This is, to the best of our knowledge, the first time such a study is carried out. To illustrate the validity of the here-presented approach, single SnO_2 nanowires have been contacted on top of non-flat substrates and their gas sensing properties have been studied and compared [30] with another, more well-established,

contacting method like dual beam focused ion beam lithography. The here-presented methodology can be adapted to contact different nanostructures on top of other unconventional substrates.

2. Experimental

Monocrystalline defect-free tin dioxide nanowires were grown by a chemical vapor deposition (CVD) process in a cold-wall quartz reactor, using Au as catalyst, as explained in detail elsewhere [31]. The precursor used is $Sn(OtBu)_4$, which is introduced into the chamber in the gas phase. Previously, a Au layer of 3-5 nm thickness is sputter-deposited, which forms nanoclusters when the temperature is raised. The NWs are grown on oxidised Si or Al_2O_3 substrates, at a temperature around 700 ºC.

After the growth, the nanowires were removed from the substrate by sonicating them while immersed in a solvent, either ethanol, isopropanol (IPA), ethylene glycol or toluene. Next, a drop of the solvent, of about 20 µl, containing the removed NWs, was deposited on top of the suspended substrates and the solvent was allowed to dry. The NWs remained, thus, randomly oriented on the surface of the substrate and the electrical contacts could be fabricated ad hoc for each nanowire subsequently.

The substrates employed for this work were micromembranes and microhotplates (micro-sized thin structures that contain a buried heater and surface electrodes) both fabricated employing bulk micromachining of Si substrates (see Fig. 1a) and b)). They are widely used as substrates for gas sensing purposes thanks to their reduced dimensions that allow them to provide locally temperatures of several hundreds of °C on the membrane with a low power consumption (in the range of mW), while keeping the rest of the substrate cold. Microhotplates, shown in Fig. 1 a), are free-standing structures, only supported by thin arms that thermally isolate them from the bulk, while micromembranes are thin closed structures (i.e. the entire perimeter of the membrane is attached to the thicker substrate, Fig. 1 b)). In this work, the thickness of both structures was about 1.1 µm. For their fabrication, first, a layer of 0.3 µm of Si_3N_4 was used as a dielectric layer, in which the heater was embedded. The heater was made either from doped polysilicon for the micromembranes or from Pt for the microhotplates. On top, 800 nm of SiO_2, with electrical isolation purposes and which covers the heater, was deposited, while the upper contacts consisted of deposited Ti/Pt interdigitated electrodes, with 25/150 nm nominal thickness in the case of micromembranes, and 25/250 nm thickness for the microhotplates, defined by a lift-off process. These electrodes were used to provide the electrical contact to the nanostructures to be measured. The active area was 100 x 100 μm^2 for both the microhotplates and micromembranes. The microhotplate required a power supply of 6 mW to reach a temperature of 350 °C, while the value is 8 mW for each heater of the micromembrane.

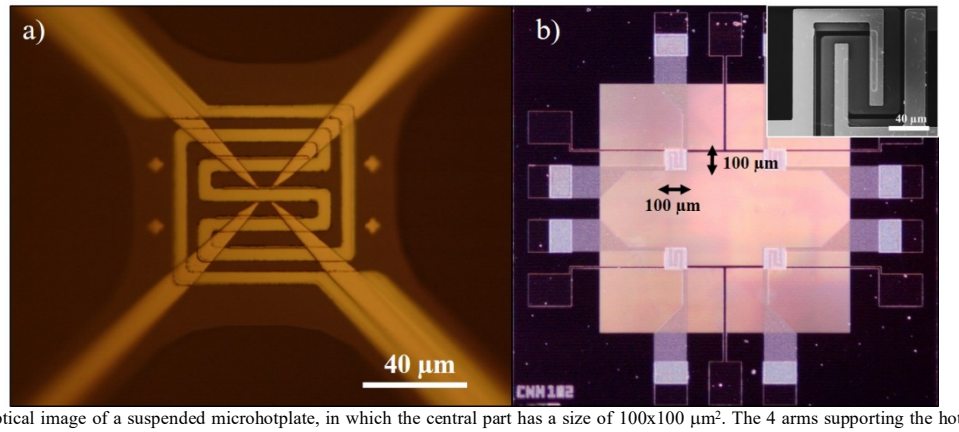

Fig. 1 a) Optical image of a suspended microhotplate, in which the central part has a size of 100x100 µm^2. The 4 arms supporting the hotplate contain electrodes accessing the centre of the microhotplate and 2 of them allow the access to the buried heater, seen as a meander in the image. Note that the 4 alignment marks (crosses) used in EBL can be clearly seen. b) Optical image of a micromembrane of 1.15x1.15 mm^2. In the membrane (light pink), 4 heaters have been fabricated below the interdigitated electrodes, located on the front side. The inset is an SEM image, showing the active area (100 x 100 µm^2) with the interdigitated electrodes and where the heater can be identified as a meander. Both structures have been fabricated using bulk micromachining techniques.

The photoresist employed in this work was 7% poly(methyl methacrylate) (PMMA) diluted in anisole (950k A7, purchased from MicroChem), which is a positive tone resist. Following the spin-coating process, the resist was soft baked at 180 °C for 1 minute. The exposure of the photoresist was performed in a Raith150 Two machine, operated at 20 kV, and with a current ranging from 100 to 600 pA. The scanned area was kept constant in the experiments, being 100 x 100 µm^2. This was large enough to avoid the need of stitching because the whole exposed pattern was kept within this writing field. After the exposure, the photoresist was developed using a mixture of methyl isobutyl ketone (MIBK) and isopropyl alcohol (1:3) for 30 s. The developer was stopped in isopropyl alcohol for additional 30 s.

The metal layers deposited on the developed substrate were a stack of Ti (20 nm) and Pt (80 nm), deposited either by e-beam evaporation or magnetron sputtering. This value was selected in this work to assure that the NWs would be completely covered by the metal, assuring an optimal contact. The dimensions of the fabricated contacts range from 10 to 50 µm in length, and 1-10 µm in width, since the contacts are designed *ad hoc* to each device.

Subsequently, the lift-off process was performed by immersing the samples in acetone for several minutes at room temperature, which assured the complete dissolution of the photoresist. It is important to mention that no ultrasounds were used during the lift-off process to avoid damaging the suspended microstructures. Finally, samples were submerged again in IPA to clean the devices from potential remaining resist impurities, followed by a soft nitrogen blow-dry.

To inspect the photoresist on the surface of the suspended substrate, confocal microscopy images of the microstructures were obtained on a Leica DCM 3D system. To measure the electrical characteristics of the devices, a Keithley 2602-A instrument equipped with two source-measurement units (SMU) was used, forcing a constant current of 1 nA. The upper limit of measurable resistance values by the mentioned equipment under those conditions is approximately 15 GΩ. High impedance measurements have been corrected considering the input impedance of the instrument. To test their functionality as sensors, the devices were bonded to a TO8 holder and then mounted in a homemade stainless steel chamber of 8.6 ml, in which a gas mixture was injected at a flow rate of 200 ml/min, using a gas mixer Gometrics MGP2. Electrical measurements and flowing gases were controlled by a home-developed Labview software. To perform the cross-section analysis of the photoresist

shape and thickness on the suspended structures, a FEI Dual-Beam Strata 235 Focused Ion Beam, equipped with a Ga ion source, was used.

3. Results and discussion

3.1 Resist profile on microhotplates and micromembranes

A crucial aspect for a successful exposure in EBL is the uniformity and flatness of the spin-coated resist. Thickness and resist height differences throughout the sample may lead to an incomplete exposure of the thicker resist regions and to an uncontrolled electron dose due to a defocused electron spot, both giving rise to non-reliable and non-reproducible lithography patterns. These effects are stronger when working with small chips due to the added edge effects during the resist spinning, which give rise to accumulation of photoresist at the edges of the spun substrates. In our case, the chips containing the microhotplates and the micromembranes had sizes of 1.2 x 3.4 mm^2 and 4 x 4 mm^2, respectively. In order to reduce the edge effect during spin-coating, a stainless steel holder for the chips was fabricated (Fig. 2 c)). As shown in the figure, the upper surfaces of the chip and of the holder were at the same height. Thus, the resist could easily be extended over the whole surface of the holder in a manner that the edge effect would mostly appear at the edges of the stainless steel holder. This simple solution significantly reduced the problem of spinning on non-flat substrates, related to the edge effect.

As explained above, since both the micromembranes and the microhotplates contained embedded heaters and top electrodes, irregularities at their surface were expected, which would affect the uniformity of the spin-coated resist. For this reason, prior to any resist spinning study, the topography of the active area of the microhotplates was analysed by confocal microscopy, as shown in Fig. 2 a). For this, the whole chip was sputter-covered with a very thin Au layer of about 10 nm to enhance the reflection of the upper transparent SiO_2 surface, which was required in confocal profilometry. The topography of the four upper electrodes and the meanders of the heater can be clearly observed in the image, in which the suspended membrane presented a significant curvature, forming an upwards bow, with a maximum height difference in the central part, compared to the wafer's surface, of around 12 µm. This was attributed to the residual mechanical stresses remaining in the structure after the bulk micromachining fabrication process, consequence of the internal stresses of the different layers, and which lead the spun resist to accumulate at the edges of the suspended membrane, giving rise to a thinner layer in the central part of the devices.

The line profile along the black line depicted in Fig. 2 a) is shown in Fig. 2 b), which gives additional local information about the topography resulting from the underlying heater. The 7 protrusions created by this heater, that extended throughout the central part of the suspended membrane, followed the shape of the heater, and protruded, approximately, 220 nm each. These protrusions, together with the curvature of the membrane, compromised the uniformity of PMMA when spin-coated, which was a critical issue that had to be examined. Additionally, but not shown in Fig 2 b), one must take into account the height of the surface electrodes, about 175 nm (indicated by an "E" in Fig. 2 a), which gave a maximum local height difference of about 400 nm.

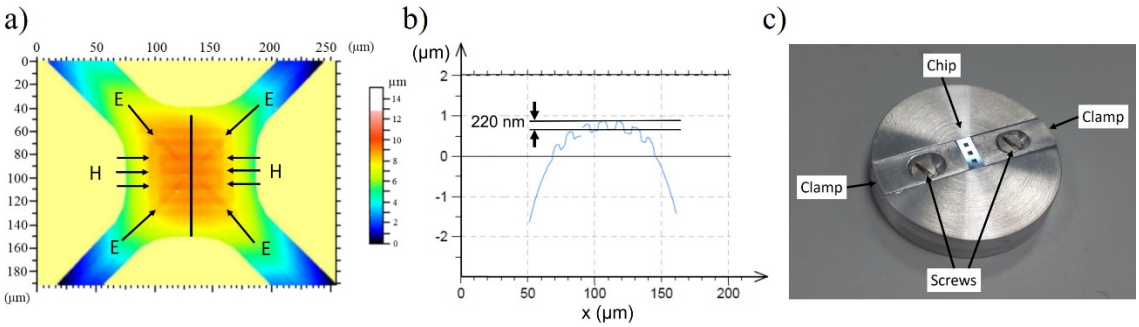

Fig. 2. a) Topographic image from the central part of the membrane obtained by confocal microscopy. The membrane is curved upwards, in which the heater (H) and electrodes (E) are visible due to the distinct height at which they are found. b) Surface profile along the line indicated in a). The 7 tracks of the heater, crossed by the drawn line, present each a height difference of about 220 nm. Note that the x- and y-axes are represented in a different scale than the z-axis. c) Image of the holder used to extend the effective area at which the resist is deposited during the spin-coating process. Diameter: 2 cm.

Table 1 Thickness of the PMMA resist obtained on top of microhotplates at different spin speeds.

Spin speed (rpm)	Thickness on top of heater (nm)	Thickness with no underlying heater (nm)
3000	400 - 450	550 - 600
4000	270 - 320	370 - 440
4500	230 - 290	330 - 400

To sum up, the microsubstrates presented (1) internal edges arising from the open structures, (2) surface bending as a result of residual mechanical stresses of the membrane/hotplates and (3) surface roughness due to the heater and surface electrodes.

To analyse in depth the profile of the spun PMMA layer and the variations in its thickness, a cross-section of the spin-coated resist was performed inside a Focused Ion Beam machine, using the Ga ion beam. Three different spin processes, employing steady velocities between 3000 and 4500 rpm for 1 minute, were studied. PMMA was always soft-baked for 1 minute at 180°C, followed by the sputtering of a thin Au layer to facilitate the observation of the PMMA layer under a confocal microscope. The measured thicknesses as a function of the spin speed are summarized in Table 1. As described in the table, thickness changed along the surface of the micromembrane.

It is important to notice that, according to the technical notes of the supplier, the expected resist thickness for the selected spinning speed is about 600 nm [32]. The most important contribution to the varying thickness of the PMMA layer was caused, as shown in Fig. 3, by the heater, and to a smaller extend, by the electrodes. The height differences of about 220 nm at the microhotplate's surface prior to the deposition was reduced to about 100 nm after spinning the PMMA coating. This effect was taken into account in the fabrication of the contacts: to minimize the variations if the PMMA thickness, it was more convenient to fabricate the EBL contacts along the heater meander than across that.

Furthermore, SEM cross-section images taken in the outer part of the membranes show that, within the experimental uncertainty, the PMMA layer had the same thickness as in the central part. In addition, measurements carried out on other membranes from the same chip and from other chips showed no appreciable changes in thickness, confirming that the use of the stainless-steel holder strongly reduced the edge effect in the chip and proved the repeatability of the method.

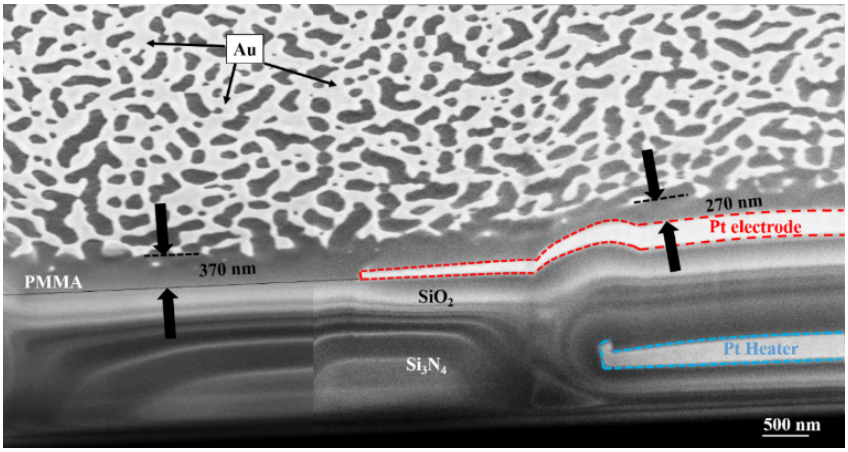

Fig. 3. Cross-section SEM image of the central area of a suspended microhotplate with spin-coated PMMA on the top. The heater gives rise to a thinner resist on top of it, and the area between the heater lines involves a thicker PMMA layer. The scale and the thickness are compensated for the tilt of the sample, which is 52°.

3.2 Optimization of the fabrication parameters

In addition to the surface topography, the thickness of the NWs played also a very important role in the feasibility of the here-presented approach. In our case, the diameter of the NWs ranged between 50 and 80 nm. Consequently, in order to ensure the full coverage of the nanowires by the metal deposition, this had to be thicker than the nanowire's diameter. Thus, in this experiment we selected a metal thickness of 100 nm. To ensure a successful lift-off process, a rule of thumb tells that the resist thickness should be, at least, a factor 3 larger than the metal thickness. This brought the required resist thickness to, at least, 300 nm.

The appropriate spin coating conditions of the PMMA photoresist were studied by varying the spinning speed between 3000 and 4500 rpm for 1 minute, followed by a soft bake at 180°C for 1 minute. Next, the samples were mounted in the EBL machine, the designed patterns were exposed and the resist was developed. Subsequently, a 20 nm thick Ti adhesion layer, followed by a 80 nm thick Pt layer, were sputter-deposited on the samples. A lift-off process, consisting in the immersion of the sample in acetone, finalized the fabrication procedure.

Regarding the PMMA spinning result, it was observed that at speeds below or equal to 3000 rpm the PMMA was too thick, which resulted in an incomplete exposure of the photoresist. This caused that most part of the fabricated contacts were removed during the lift-off step. Further increasing the electron dose was not effective in circumventing this problem. When spinning at 4500 rpm, lift-off was non-reproducible, since it failed to completely remove the metal everywhere in the sample, possibly due to thin resist residues. The most appropriate conditions for the PMMA deposition, in terms of a successful exposure and lift-off, were found to be 4000 rpm for 1 minute, which lead to a PMMA thickness around 300 nm on top of the meanders and 400 nm, elsewhere.

Under these optimal conditions, the effect of the electron dose was also studied. According to the data sheet [32], the range of doses was set according to the recommendations of the supplier from 50 to 500 μC/cm^2 (the usual values employed in our laboratory for bulk Si substrates being 100 μC/cm^2). Our results showed that for doses up to 300 μC/cm^2, bad adhesion of the metal layers on top of the PMMA occurred, and that the PMMA is further removed (or partially peeled off) during the lift-off process. Most probably this is because the bottom PMMA resist layer was not sufficiently exposed, as shown in Figs. 4 a) and b), corresponding to a microhotplate and a micromembrane, respectively, exposed at 100 μC/cm^2. Similar results were obtained at 300 μC/cm^2. For the optimised PMMA photoresist thickness, a complete exposure of the resist and thus, a good adhesion of the metal layers, was achieved using an electron dose of 600 μC/cm^2 or above. The images of the fabricated contacts using this dose are presented in Figs. 4 c) and d), corresponding to the same type of substrates shown in Figs. 4 a) and b), respectively. The most likely reason for the need of this higher electron dose to define a pattern in our micromachined platforms, in comparison with bulk Si substrates, was the reduced thickness of the former, which resulted in a much lower number of back scattered electrons due to the absence of underlying silicon substrate [33]. This is an important result to be considered when extending this methodology to other suspended substrates with different thickness as the ones employed here, which might require an even higher dose for thinner substrates.

The electrical characterization of the titanium and platinum deposits in correctly spun and exposed samples was performed by defining linear patterns connecting two of the top electrodes. The measured resistance values were below 300 Ω and the exact value depended on the length and width of the contacts. The average metal resistivity measured in these samples was of 25±6 μΩ·cm, which is between the bulk resistivity of Pt (9.76 μΩ·cm) and of Ti (41.8 μΩ·cm) [34]**.** For practical applications, it is important that the resistance of the EBL-fabricated metal contacts is orders of magnitude lower than the resistance of the material to be contacted. In our case, the resistance of individual SnO_2 nanowires ranges usually between hundreds of kΩ and hundreds of MΩ [16]. This assures that the contribution of the contacts on the overall measured resistance of the gas sensors is negligible.

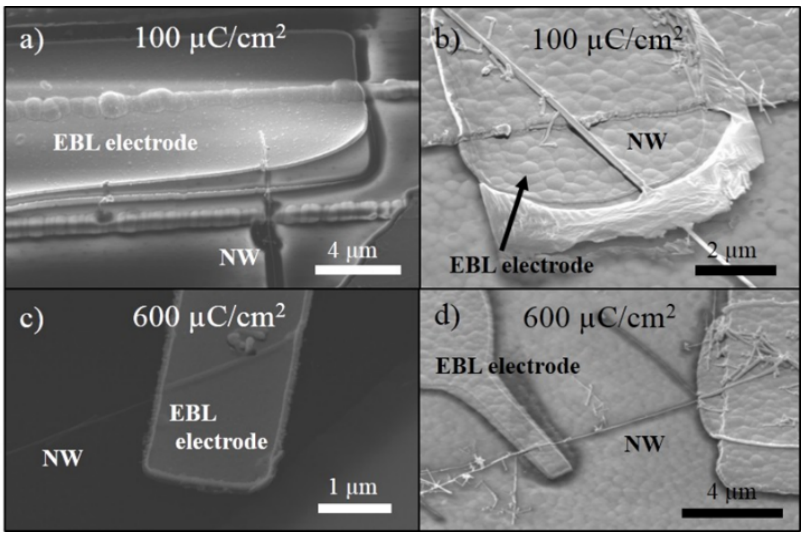

Fig. 4. SEM images of the Ti/Pt contacts fabricated by EBL. a) c) on a suspended microhotplate, and b) d) on a micromembrane. A bad adherence due to the remaining resist, which is caused by an incomplete exposure, is shown in a) and b), exposed with an electron dose of 100 μC/cm^2. For a complete exposure, as shown in c) and d), a much higher electron dose has been required (600 μC/cm^2).

3.3 Fabrication and characterization of devices based on individual nanowires

The gas nanosensors were fabricated starting by drop casting the NWs onto the suspended platforms. Next, the samples were introduced in the EBL system and the NWs were localized with the electron microscope, employing prepatterned alignment marks which were introduced during the fabrication processes of the micromembrane and microhotplate. The contacts were designed *ad-hoc* for each nanowire. The samples were then removed from the EBL chamber, the photoresist was spun on and the samples were transferred back into the EBL chamber, where the alignment marks were localized and the designed patterns were exposed onto the photoresist.

SEM pictures of two different SnO_2 NWs with EBL-fabricated contacts are shown in Fig. 5. A single NW, contacted on top of a microhotplate (with a diameter of 50 ± 3 nm) is shown in Figs. 5 a) and b). The NW on Fig. 5 c) (with a diameter of 55 ± 4 nm) was contacted on top of a micromembrane, which is shown in higher magnification images in Figs. 5 d) and e). The magnified images in Figs. 5 b), d) and e) show the fabricated contacts, which prove the full coverage of the NW contact region that could later be used to carry out electrical measurements.

3.3.1 Electrical characterization of the contacted nanowires

The contacted nanowires were electrically characterized at different temperatures to determine the type of contact formed between the metals and the NW (Fig. 6). The experimental curves clearly showed a non-linear behaviour for the Pt/Ti/SnO_2/Ti/Pt structures, for which an ohmic behaviour would be preferred (i.e. a linear current-voltage curve).

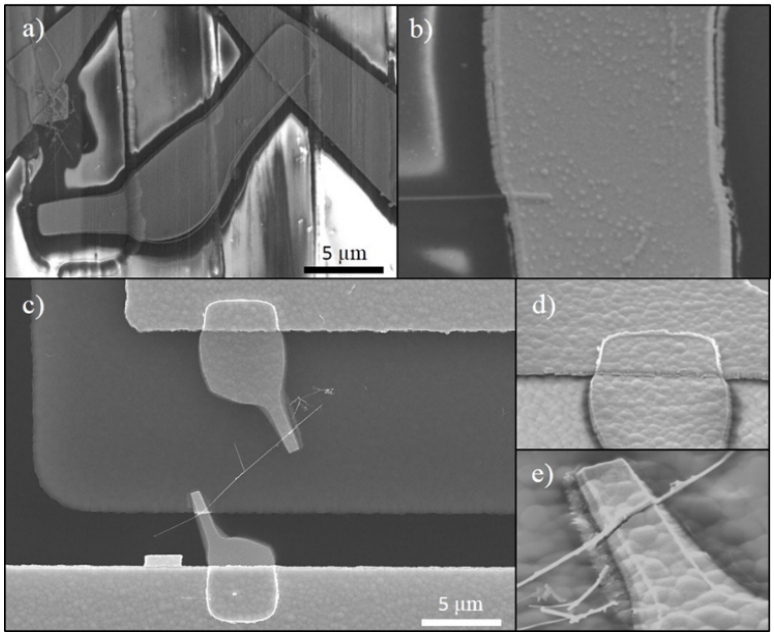

Fig. 5 SEM pictures of the individual SnO_2 NWs contacted on top of a) a microhotplate and c) a micromembranes. b) Zoom into the lower contact of a). d) and e) are zoomed into the upper and lower contacts, respectively. The metal patterns defined by EBL clearly cover the NW and the slope caused by the electrode from the microplatform, suggesting a good electrical contact.

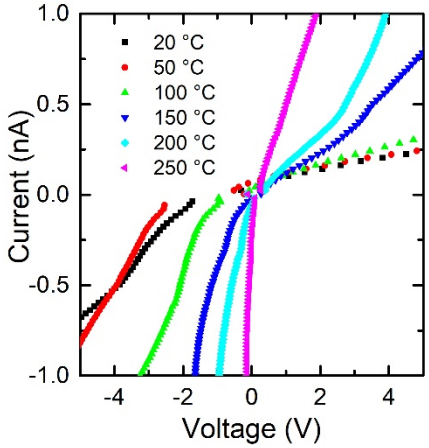

Fig. 6. I-V curves at different temperatures from a SnO_2 NW contacted by EBL on top of a microhotplate

In this sense, the contact between a metal and a semiconductor can introduce a Schottky barrier for the charge carriers crossing that junction, giving rise to an exponential current-voltage dependence like the one observed in Fig. 6. In this case, the effective barrier height, the so-called built-in potential eV_{bi} at a metal/n-type semiconductor junction (which is the case of SnO_2 nanowires), is defined as the difference between the work function of the metal (ϕ_m) and electron affinity of the semiconductor (χ_s):

$$eV_{bi} = \phi_m - \chi_s \qquad (1)$$

Since titanium has a low work function (3.84 eV), and the electron affinity of SnO_2 is around 4.74 eV [35], no barrier would be expected, which is estimated to result in an ohmic behaviour. The observed non-Ohmic behaviour might be attributed either to the oxidation of the Ti layer at the interface, or to chemical residues at the semiconductor/metal interface originated from the organic solvents used during the spin-coating of PMMA and the lift-off process. Both phenomena would create surface states that would modulate the junction barrier, likely promoting the high resistance observed on the experimental measurements.

As expected theoretically, the rectifying behaviour was reduced with increasing temperature and approached the Ohmic characteristics (see measurements at 250°C in Fig. 6). In order to improve the quality of the contacts and achieve low resistance Ohmic contacts, an oxygen plasma cleaning process could be considered after the development of the resist and before the deposition of the metals [36], but has not been employed in this work.

3.3.2 Chemical sensing response towards NH_3

The gas response of the individual, EBL-contacted SnO_2 NWs was studied towards different concentrations of ammonia diluted in air. For this, the NWs were exposed to alternating pulses of different concentrations of ammonia diluted in dry air at different temperatures, as shown in Fig. 7 a). While the n-type metal oxide nanowire is in contact with dry air, oxygen molecules are adsorbed at its surface and are dissociated into atomic oxygen, which occurs with the capture of electrons from the semiconductor. When this surface is next exposed to ammonia, its adsorption occurs together with its oxidation with the preadsorbed oxygen species, leading to oxygen desorption from the SnO_2 and releasing the electrons back to the metal oxide. As a consequence, the resistance of the semiconductor is reduced, which is clearly observed in Fig. 7 a). All this is in agreement with data published in literature [37]**.** This reduction is larger the higher the ammonia

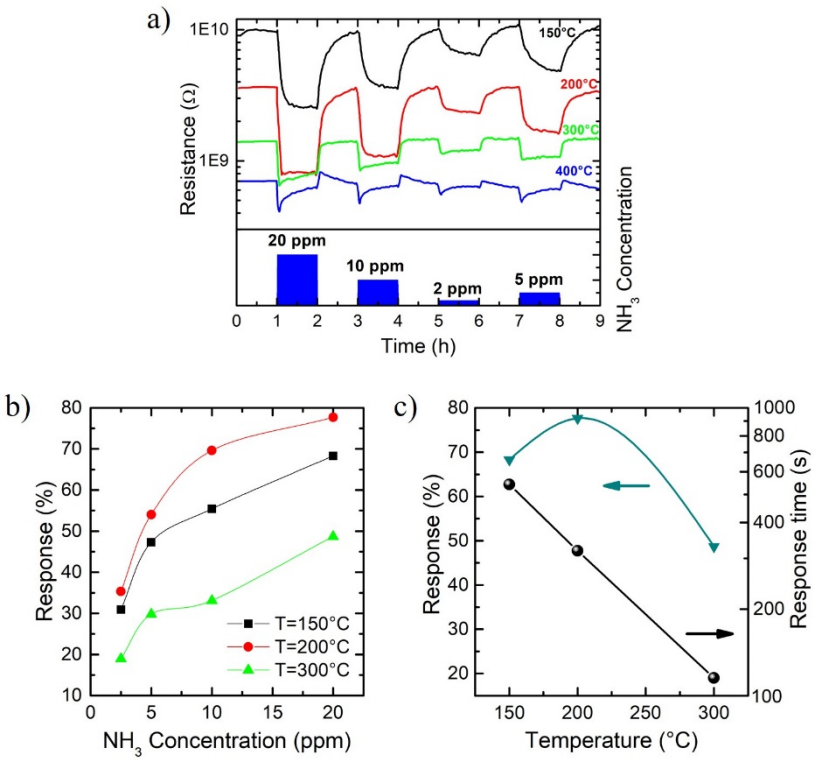

Fig. 7 a) Resistance change of individual NWs towards different ammonia concentration exposures for 1 hour, at temperatures between 150 and 400ºC; b) Measured ammonia gas sensing response represented as a function of the concentration. The response obtained at 400°C is not shown due to the abnormal behaviour caused by side reactions interfering the measurement; c) Plot of the response (left axis) and Arrhenius plot of the response time (right axis) as a function of temperature for 20 ppm of NH_3.

concentration, as observed in the same figure, which proves the sensing behaviour of the device. For practical applications, it is important that the NW recovers its original resistance baseline after removing ammonia from the ambience and this is also clearly seen in Fig. 7.

In gas sensing applications, a common way to define the gas response is as follows:

$$Response(\%) = (R_{air} - R_{NH_3})/R_{air} \quad (2)$$

where R_{air} is the resistance in the presence of dry synthetic air and R_{NH3}, in presence of a certain amount of ammonia diluted in air. The steady state response of the nanowire as a function of ammonia concentration is represented in Fig. 7 b), and as a function of the temperature for 20 ppm of NH_3 is represented in Fig. 7 c). In metal-oxide sensors, this response depends on the temperature, showing the typical bell shape [30]. According to well stablished models, this behaviour is attributed to the opposite temperature dependence of the adsorption, diffusion and desorption of oxygen, ammonia and other gas species. In this case, these effects are balanced (i.e. the response is maximized) at approximately 200 °C, reaching a response value of 75% at 20 ppm of NH_3.

The response time of the sensor, defined as the time to evolve from the 10% to the 90% of the steady state response value (Fig. 7 c), decreased exponentially with temperature, following an Arrhenius-type trend. Response times under 2 minutes at 300 °C were measured in the experiments with ammonia.

The nanowire's resistance at 400 °C dropped immediately after ammonia entered into the measuring chamber, followed by a slow rise, which almost cancelled the response of the NW. Such behaviour was also observed, to a lower extent, at 300 °C. For this reason, the result at 400 °C was not included in the figure of the sensor's response, Fig. 7 c). The same

trend was observed in other resistive gas sensors based on nano-WO_3 powders [38] or meshes of SnO_2 NWs [10]**.** Compared to these works, the effect is more pronounced in the EBL-contacted NW. In the here-presented results, the response is not only reduced but almost suppressed. According to previous works [10], this effect is caused by the promotion of nitric oxide as a byproduct of the ammonia oxidation by the chemisorbed oxygen at the surface of the nanowire, which occurs at high temperatures.

The results obtained in this work were compared with those from sensors based on individual SnO_2 NWs, contacted using a FIB-based technique, which showed a maximum response at 250 °C of about 40% for 100 ppm [37] and about 30% for 25 ppm has been reported [39]. The results obtained in the present work with the EBL-fabricated sensors show a significantly higher response, namely 70% of resistance variation at 20 ppm of NH_3 at 200 °C, as already stated.

Regarding the response times, previous works reported values from 50 s [37] to 15 min [39] for 100 ppm of NH_3. Our device presented times around 5 minutes for 20 ppm of NH_3 at 200 °C. Although this value is higher than the one reported above [37]**,** it is important to note that for concentrations of 100 ppm of ammonia, shorter response times are expected, due to a quicker response of sensors with rising gas concentration [40].

3.4 Comparison with other methods and further applications

Comparing the EBL approach to the FIB-related one, the here presented method offers important reduction in the fabrication time, due to the higher throughput of EBL. Also, the better conductivity of the EBL-fabricated contacts leads to more robust and stable devices (e.g. less Joule heating at the contacts). Furthermore, unlike FIB deposition-assisted contacts, the EBL contacts are carbon-free, which provides better chemical stability when operating at 400 °C or above, allowing an extension of the operating temperature when compared to FIB deposition.

The detailed fabrication process described was demonstrated for nanowires with a diameter up to 80 nm. Thicker nanowires will require thicker metal layers and will, thus, demand thicker PMMA layers, which might not be completely exposed unless higher acceleration voltages are used (>30 kV). The parameter optimization procedure presented in this paper can be tailored to attain the optimal conditions for experiments with other EBL equipment and substrate features.

4. Conclusions

In this work, a methodology for the fabrication of contacts by electron beam lithography to individual SnO_2 nanowires on top of suspended microhotplates and micromembranes has been presented. The difficulties originating from a significant buckling of suspended structures and strong surface roughness caused by the buried heater and surface electrodes have been addressed. The photoresist spinning conditions and the electron doses required to expose the photoresist correctly have been optimized to obtain adequate electrical contact to the nanowires.

The devices have been tested against the presence of ammonia and the measured resistance variations followed the expected dependence reported for other SnO_2 devices, with an optimal response at a temperature of about 200°C. Compared with similar nanowire integration techniques (e.g. Focused Electron Beam technologies), the nanosensors described herein show an improved response and a shorter response time.

The here-presented fabrication methodology can be easily adapted to other nanostructures, like nanotubes or nanorods, and to unconventional substrates with different thicknesses, structuring, roughness and shapes.

Acknowledgements

This work has been partially supported by the Spanish Ministerio de Economía y Competitividad, through projects TEC2013-48147-C6 and TEC2016-79898-C6 (AEI/FEDER, EU) and by the European Research Council, under the European Union's Seventh Framework Program (FP/2007-2013) / ERC Grant Agreement n. 336917. J.D. Prades acknowledges the support of the Serra Húnter Program. Part of this work has been carried out through a STSM within the COST project TD1105.

References

[1] P. Yang, R. Yan, M. Fardy, Semiconductor Nanowire: What's Next?, Nano Lett. 10 (2010) 1529–1536. doi:10.1021/nl100665r.

[2] Q. Cao, J.A. Rogers, Ultrathin Films of Single-Walled Carbon Nanotubes for Electronics and Sensors: A Review of Fundamental and Applied Aspects, Adv. Mater. 21 (2009) 29–53. doi:10.1002/adma.200801995.

[3] S. Barth, F. Hernandez-Ramirez, J.D. Holmes, A. Romano-Rodriguez, Synthesis and applications of one-dimensional semiconductors, Prog. Mater. Sci. 55 (2010) 563–627. doi:10.1016/j.pmatsci.2010.02.001.

[4] UNESCO Global Science Report: Towards 2030, UNESCO Publishing, Paris, 2015.

[5] C.M. Hung, D.T.T. Le, N. Van Hieu, On-chip growth of semiconductor metal oxide nanowires for gas sensors: A review, J. Sci. Adv. Mater. Devices. 2 (2017) 263–285. doi:https://doi.org/10.1016/j.jsamd.2017.07.009.

[6] L. Chen, W. Lu, C.M. Lieber, Chapter 1 Semiconductor Nanowire Growth and Integration, in: Semicond. Nanowires From Next-Generation Electron. to Sustain. Energy, The Royal Society of Chemistry, 2015: pp. 1–53. doi:10.1039/9781782625209-00001.

[7] Y. Chen, Nanofabrication by electron beam lithography and its applications: A review, Microelectron. Eng. 135 (2015) 57–72. doi:10.1016/j.mee.2015.02.042.

[8] H.Y. Tuan, D.C. Lee, T. Hanrath, B.A. Korgel, Catalytic solid-phase seeding of silicon nanowires by nickel nanocrystals in organic solvents, Nano Lett. 5 (2005) 681–684. doi:10.1021/nl050099d.

[9] S. Barth, R. Jimenez-Diaz, J. Samà, J. Daniel Prades, I. Gracia, J. Santander, C. Cane, A. Romano-Rodriguez, Localized growth and in situ integration of nanowires for device applications, Chem. Commun. 48 (2012) 4734–4736. doi:10.1039/c2cc30920c.

[10] J. Samà, S. Barth, G. Domènech-Gil, J.-D. Prades, N. López, O. Casals, I. Gràcia, C. Cané, A. Romano-Rodríguez, Site-selectively grown SnO_2 NWs networks on micromembranes for efficient ammonia sensing in humid conditions, Sensors Actuators B Chem. 232 (2016) 402–409. doi:10.1016/j.snb.2016.03.091.

[11] K. Chikkadi, M. Muoth, V. Maiwald, C. Roman, C. Hierold, Ultra-low power operation of self-heated, suspended carbon nanotube gas sensors, Appl. Phys. Lett. 103 (2013) 223109. doi:10.1063/1.4836415.

[12] M.N. Cardoza-Contreras, J.M. Romo-Herrera, L.A. Ríos, R. García-Gutiérrez, T.A. Zepeda, O.E. Contreras, Single ZnO Nanowire-Based Gas Sensors to Detect Low Concentrations of Hydrogen, Sensors. 15 (2015) 30539–30544. doi:10.3390/s151229816.

[13] O. Lupan, V. Postica, F. Labat, I. Ciofini, T. Pauporté, R. Adelung, Ultra-sensitive and selective hydrogen nanosensor with fast response at room temperature based on a single Pd/ZnO nanowire, Sensors Actuators B Chem. 254 (2018) 1259–1270. doi:https://doi.org/10.1016/j.snb.2017.07.200.

[14] F. Hernandez-Ramirez, J.D. Prades, A. Tarancon, S. Barth, O. Casals, R. Jimenez-Diaz, E. Pellicer, J. Rodriguez, J.R. Morante, M.A. Juli, S. Mathur, A. Romano-Rodriguez, Insight into the role of oxygen diffusion in the sensing mechanisms of SnO_2 nanowires, Adv. Funct. Mater. 18 (2008) 2990–2994. doi:10.1002/adfm.200701191.

[15] G. Domènech-Gil, S. Barth, J. Samà, P. Pellegrino, I. Gràcia, C. Cané, A. Romano-Rodriguez, Gas sensors based on individual indium oxide nanowire, Sensors Actuators B Chem. 238 (2017) 447–454. doi:http://dx.doi.org/10.1016/j.snb.2016.07.084.

[16] F. Hernández-Ramírez, A. Tarancón, O. Casals, J. Rodríguez, A. Romano-Rodríguez, J.R. Morante, S. Barth, S. Mathur, T.Y. Choi, D. Poulikakos, V. Callegari, P.M. Nellen, Fabrication and electrical characterization of circuits based on individual tin oxide nanowires., Nanotechnology. 17 (2006) 5577–5583. doi:10.1088/0957-4484/17/22/009.

[17] M.S. Arnol, P. Avouris, Z. Wei Pan, Z.L. Wang, Field-Effect Transistors Based on Single Semiconducting Oxide Nanobelts, J. Phys. Chem. B. 107 (2003) 659–663. doi:10.1021/jp0271054.

[18] D. Kälblein, R.T. Weitz, H.J. Böttcher, F. Ante, U. Zschieschang, K. Kern, H. Klauk, Top-Gate ZnO Nanowire Transistors and Integrated Circuits with Ultrathin Self-Assembled Monolayer Gate Dielectric, Nano Lett. 11 (2011) 5309–5315. doi:10.1021/nl202767h.

[19] X. Jiang, Q. Xiong, S. Nam, F. Qian, Y. Li, C. M. Lieber, InAs/InP Radial Nanowire Heterostructures as High Electron Mobility Devices, Nano Lett. 7 (2007) 3214–3218.

doi:10.1021/nl072024a.
[20] P. Feng, F. Shao, Y. Shi, Q. Wan, Gas Sensors Based on Semiconducting Nanowire Field-Effect Transistors, Sensors (Basel). 14 (2014) 17406–17429. doi:10.3390/s140917406.
[21] P. Durina, A. Bencurova, A. Konecnikova, I. Kostic, K. Vutova, E. Koleva, G. Mladenov, P. Kus, A. Plecenik, Patterning of structures by e-beam lithography and ion etching for gas sensor applications, J. Phys. Conf. Ser. 514 (2014) 12037.
[22] P. Candeloro, A. Carpentiero, S. Cabrini, E. Di Fabrizio, E. Comini, C. Baratto, G. Faglia, G. Sberveglieri, A. Gerardino, SnO_2 sub-micron wires for gas sensors, Microelectron. Eng. 78–79 (2005) 178–184. doi:10.1016/j.mee.2004.12.024.
[23] S.N. Das, J.P. Kar, J.-H. Choi, T. Il Lee, K.-J. Moon, J.-M. Myoung, Fabrication and Characterization of ZnO Single Nanowire-Based Hydrogen Sensor, J. Phys. Chem. C. 114 (2010) 1689–1693. doi:10.1021/jp910515b.
[24] A. Köck, L. Chitu, S. Defregger, E. Kraker, G. Maier, S. Steinhauer, R. Wimmer-Teubenbacher, Metal Oxide Nanowires for Gas Sensor Applications, BHM Berg- Und Hüttenmännische Monatshefte. 159 (2014) 385–389. doi:10.1007/s00501-014-0286-5.
[25] L. Liao, Z. Zheng, B. Yan, J.X. Zhang, H. Gong, J.C. Li, C. Liu, Z.X. Shen, T. Yu, Morphology Controllable Synthesis of α-Fe_2O_3 1D Nanostructures: Growth Mechanism and Nanodevice Based on Single Nanowire, J. Phys. Chem. C. 112 (2008) 10784–10788. doi:10.1021/jp802968a.
[26] A. Varea, S. Pane, S. Gerstl, M.A. Zeeshan, B. Ozkale, B.J. Nelson, S. Surinach, M.D. Baro, J. Nogues, J. Sort, E. Pellicer, Ordered arrays of ferromagnetic, compositionally graded $Cu_{1-x}Ni_x$ alloy nanopillars prepared by template-assisted electrodeposition, J. Mater. Chem. C. 1 (2013) 7215–7221. doi:10.1039/C3TC31310G.
[27] O. Chmela, J. Sadilek, G. Domenech-Gil, J. Sama, J. Somer, R. Mohan, A. Romano-Rodriguez, J. Hubalek, S. Vallejos, Selectively arranged single-wire based nanosensor array systems for gas monitoring, Nanoscale. 10 (2018) 9087–9096. doi:10.1039/C8NR01588K.
[28] F. Yang, S.-C. Kung, M. Cheng, J.C. Hemminger, R.M. Penner, Smaller is Faster and More Sensitive: The Effect of Wire Size on the Detection of Hydrogen by Single Palladium Nanowires, ACS Nano. 4 (2010) 5233–5244. doi:10.1021/nn101475c.
[29] M. Afshar, E.M. Preiß, T. Sauerwald, M. Rodner, D. Feili, M. Straub, K. König, A. Schütze, H. Seidel, Indium-tin-oxide single-nanowire gas sensor fabricated via laser writing and subsequent etching, Sensors Actuators B Chem. 215 (2015) 525–535. doi:https://doi.org/10.1016/j.snb.2015.03.067.
[30] P.T. Moseley, Solid state gas sensors, Meas. Sci. Technol. 8 (1997) 223–237. doi:10.1088/0957-0233/8/3/003.
[31] S. Mathur, S. Barth, H. Shen, J.-C. Pyun, U. Werner, Size-Dependent Photoconductance in SnO_2 Nanowires, Small. 1 (2005) 713–717. doi:10.1002/smll.200400168.
[32] MicroChem, PMMA Data Sheet, 2001.
[33] A.N. Broers, Resolution Limits of PMMA Resist for Exposure with 50 kV Electrons, J. Electrochem. Soc. 128 (1981) 166–170. doi:10.1149/1.2127360.
[34] J. Bass, 1.2.1 Pure metal resistivities at T = 273.2 K: Datasheet from Landolt-Börnstein - Group III Condensed Matter - Volume 15A: Electrical Resistivity, Kondo and Spin Fluctuation Systems, Spin Glasses and Thermopower, (n.d.). doi:10.1007/10307022_3.
[35] J.F. Geiger, K.D. Schierbaum, W. Göpel, Surface spectroscopic studies on Pd-doped SnO_2, Vacuum. 41 (1990) 1629–1632. doi:http://dx.doi.org/10.1016/0042-207X(90)94037-Q.
[36] Y. Cheng, R. Yang, J.P. Zheng, Z.L. Wang, P. Xiong, Characterizing individual SnO_2 nanobelt field-effect transistors and their intrinsic responses to hydrogen and ambient gases, Mater. Chem. Phys. 137 (2012) 372–380. doi:10.1016/j.matchemphys.2012.09.037.
[37] D.C. Meier, S. Semancik, B. Button, E. Strelcov, A. Kolmakov, Coupling nanowire chemiresistors with MEMS microhotplate gas sensing platforms, Appl. Phys. Lett. 91 (2007). doi:10.1063/1.2768861.
[38] I. Jiménez, M. a. Centeno, R. Scotti, F. Morazzoni, A. Cornet, J.R. Morante, NH_3 Interaction with Catalytically Modified Nano-WO_3 Powders for Gas Sensing Applications, J. Electrochem. Soc. 150 (2003) H72–H80. doi:10.1149/1.1556055.
[39] F. Shao, M.W.G. Hoffmann, J.D. Prades, J.R. Morante, N. López, F. Hernández-Ramírez,

Interaction mechanisms of ammonia and Tin oxide: A combined analysis using single nanowire devices and DFT calculations, J. Phys. Chem. C. 117 (2013) 3520–3526. doi:10.1021/jp3085342.

[40] J.W. Gardner, A non-linear diffusion-reaction model of electrical conduction in semiconductor gas sensors, Sensors Actuators B Chem. 1 (1990) 166–170. doi:10.1016/0925-4005(90)80194-5.